Resonance-assisted tunneling in four-dimensional normal-form Hamiltonians

Markus Firmbach,[1,2] Felix Fritzsch,[1] Roland Ketzmerick,[1,2] and Arnd Bäcker[1,2]
[1]*Technische Universität Dresden, Institut für Theoretische Physik and Center for Dynamics, 01062 Dresden, Germany*
[2]*Max-Planck-Institut für Physik komplexer Systeme, Nöthnitzer Straße 38, 01187 Dresden, Germany*

(Received 10 January 2019; published 19 April 2019)

Nonlinear resonances in the classical phase space lead to a significant enhancement of tunneling. We demonstrate that the double resonance gives rise to a complicated tunneling peak structure. Such double resonances occur in Hamiltonian systems with an at least four-dimensional phase space. To explain the tunneling peak structure, we use the universal description of single and double resonances by the four-dimensional normal-form Hamiltonians. By applying perturbative methods, we reveal the underlying mechanism of enhancement and suppression of tunneling and obtain excellent quantitative agreement. Using a minimal matrix model, we obtain an intuitive understanding.

DOI: 10.1103/PhysRevE.99.042213

I. INTRODUCTION

Quantum tunneling connects classically disjoint regions and therefore is one of the most prominent features of quantum mechanics. In particular, the description of tunneling through energy barriers allowed for computing of molecular ground states [1] and explaining radioactive decay [2,3]. However, classical barriers may arise not only from potential barriers but can be generated by the classical dynamics in phase space, leading to the concept of dynamical tunneling [4,5]. The paradigmatic example for this is tunneling between dynamically unconnected regions of a mixed phase space in which chaotic and regular motion coexists. There, for instance, tunneling between two regular regions, separated by chaotic dynamics, is moderated by chaos-assisted tunneling through the chaotic component of phase space [6–8]. The tunneling between regular and chaotic regions is described by regular-to-chaotic tunneling [9,10]. Being a fundamental quantum mechanical effect, dynamical tunneling is of relevance in many different fields of physics, e.g., vibrational spectra of molecules [4,11,12], systems of ultracold atoms [13,14], optical microcavities [15–21], and microwave billiards [22–24], and explains power-law-level repulsion at small energy spacings in systems with mixed phase spaces [25].

The presence of nonlinear resonances can drastically enhance the tunneling between disconnected regions in phase space by the mechanism of resonance-assisted tunneling [26–28]. Under variation of a parameter, significant enhancement of tunneling is observed. This was recently demonstrated in experiments for microwave resonators [29] and optical microcavities [21] by varying the frequency or the shape of the boundary. A lot of progress has been made concerning the theoretical understanding of resonance-assisted tunneling [9,12,20,23,26–28,30–49], mostly concentrating on systems effectively described by two-dimensional (2D) maps. One of the key tools for the theoretical description is the mapping of the system with nonlinear resonances to a universal pendulum-like 2D normal-form Hamiltonian, arising from secular perturbation theory [26,28] or normal form theory [50]. The quantized normal-form Hamiltonians allow us to explain the universal features of resonance-assisted tunneling in 2D quantum maps, respectively, making them a key ingredient for a comprehensive understanding.

Dynamical tunneling and specifically resonance-assisted tunneling has also been studied in higher dimensional systems [51–55]. Generically, in such systems resonances of higher rank arise, which are not present in 2D systems. The case of rank 2 is called double resonance and is the simplest case showing these types of dynamics. It occurs in an at least four-dimensional symplectic map or 6D Hamiltonian. In the vicinity of a double resonance, the dynamics is effectively described by the interpolating flow of a 4D normal-form Hamiltonian [56–60]. Thus, studying tunneling in such 4D normal-form Hamiltonians provides a first step toward the understanding of resonance-assisted tunneling in 4D symplectic maps. Experimentally realizable systems with double resonances are, for example, three-dimensional optical microcavities or microwave resonators as well as periodically driven two-dimensional systems. Moreover, the quantized normal-form Hamiltonians have applications in the studies of vibrational dynamics of chemical molecules [11,12,61–69]. In particular, the intramolecular energy transfer is heavily influenced by classical nonlinear resonances, as they allow for couplings between different vibrational modes [11,12]. However, a quantitative description based on resonance-assisted tunneling has not been worked out so far.

In this paper, we give a qualitative as well as a quantitative description of resonance-assisted tunneling in the presence of a double resonance. To this end, we consider the classical dynamics of the simplest 4D normal-form Hamiltonians, which describe the dynamics of either a single coupled resonance or a double resonance. Subsequently, we study the phase-space localization of the eigenstates of the quantized systems in classically disjoint regions. We find that tunneling in the vicinity of the single resonance shows the same characteristics as in 2D systems, i.e., a drastic enhancement of tunneling. Such an enhancement is also seen in the case of the double

resonance but occurs in a very complex fashion. Additionally, we also observe the suppression of tunneling. Utilizing a perturbative expansion based on paths in action space, we are able to quantitatively explain the complicated peak structure of enhancement as well as suppression. This provides a first step toward a detailed understanding of resonance-assisted tunneling in higher dimensions. The application to generic 4D quantum maps is beyond the scope of this paper and remains subject of further research.

The paper is organized as follows: In Sec. II, a brief sketch of the general approach is given. By means of the instructive example of tunneling in the case of a single coupled resonance, we introduce the methods and notation in Sec. II A. Section II B treats the central case of a double resonance. For both cases, the classical normal-form model as well as the associated quantum system is investigated. Quantitatively resonance-assisted tunneling is studied by means of numerical diagonalization and a perturbative description of the underlying mechanism is presented. The key features of resonance-assisted tunneling in the normal-form Hamiltonians can be intuitively understood within a minimal 4×4 matrix model presented in Sec. II C. Finally, a summary and outlook is given in Sec. III.

II. RESONANCE-ASSISTED TUNNELING

Classical nonlinear resonances are ubiquitous in Hamiltonian dynamical systems and manifest themselves by means of resonance-assisted tunneling in the corresponding quantum system. In order to explain the quantum features based on classical properties, we utilize a universal description of the classical dynamics in terms of a truncated 4D normal-form Hamiltonian approximating both single and double resonances [56–60]. The corresponding 4D phase space is separated into dynamically disjoint regions by the resonance channels associated with the nonlinear resonances. The eigenstates of the quantum Hamiltonian predominantly localize on classical quantizing tori, located in one of these regions. However, due to tunneling, there is also nonvanishing probability in the other, classically forbidden, regions. We introduce the weight in these regions as a quantitative measure of resonance-assisted tunneling which shows similar characteristics as known from two-dimensional quantum maps [48]. A perturbative description of resonance-assisted tunneling is obtained for both single coupled resonances and double resonances. This allows for an intuitive understanding of the enhancement and, in the case of double resonances, also the suppression of tunneling in terms of perturbative paths along a discrete action grid.

A. Single coupled resonance

First, the instructive case of the single coupled resonance in a 4D Hamiltonian system is considered, which will turn out to be quite similar to 2D systems with a single dominating resonance. To this end, we start with the classical resonant Hamiltonian [56–60]

$$H(\boldsymbol{\theta}, \boldsymbol{I}) = H_0(\boldsymbol{I}) + V(\boldsymbol{\theta}) \tag{1}$$

obtained from normal-form analysis and truncation. It is expressed in action-angle coordinates $\boldsymbol{I} = (I_1, I_2)$ and $\boldsymbol{\theta} = (\theta_1, \theta_2)$ of $H_0(\boldsymbol{I})$. Keeping only the nonresonant, quadratic order gives

$$H_0(\boldsymbol{I}) = \tfrac{1}{2}(\boldsymbol{I} - \boldsymbol{I}_{\mathrm{res}})^{\mathrm{T}} \mathbf{M} (\boldsymbol{I} - \boldsymbol{I}_{\mathrm{res}}) \tag{2}$$

for some real symmetric matrix $\mathbf{M}$, such that $H_0(\boldsymbol{I})$ has an isolated extreme at $\boldsymbol{I}_{\mathrm{res}}$.

For the single resonance, the lowest order resonant term is given by $V(\boldsymbol{\theta}) = 2V_s \cos(\boldsymbol{s}\boldsymbol{\theta})$ and the resonance vector $\boldsymbol{s} = (s_1, s_2)$. By means of a canonical transformation, either the resonance vector can be brought to the form $\boldsymbol{s} = (s_1, 0)$, i.e., an uncoupled resonance, or $\mathbf{M}$ may be transformed to diagonal form. Here, we choose $\mathbf{M} = M_{\mathrm{res}}^{-1}\mathbf{1}$. Since the potential $V(\boldsymbol{\theta})$ is 2π periodic, the phase space of the system is the cylinder $\mathbb{T}^2 \times \mathbb{R}^2$. Furthermore, the system is integrable because energy is conserved and $s_2 I_1 - s_1 I_2$ is a second constant of motion called polyad number [70].

For concrete numerical calculations and visualization, we choose $\boldsymbol{s} = (1, 1)$, $V_s = 0.1$, $M_{\mathrm{res}} = 0.8$ and $\boldsymbol{I}_{\mathrm{res}} = (1.0, 1.0)$. Instead of restricting the 4D phase space to a 3D energy manifold and introducing a Poincaré section to obtain a 2D representation of the dynamics, we show the 3D hyperplane for a fixed value of $\theta_2 = 0$ and visualize the remaining three coordinates (θ_1, I_1, I_2). This allows for an intuitive representation of the phase-space structures for different energies. In Fig. 1, this hyperplane for $\theta_2 = 0$ is shown. Regular dynamics takes place on 2D tori so that they appear as 1D curves. Furthermore, the 4D phase space is foliated into invariant 3D planes of constant polyad number. In the 3D hyperplane, they appear as 2D planes resembling the dynamics of a pendulum. In Fig. 1, orbits in four such planes are shown. The stable and unstable fixed points of these pendulums correspond to elliptic and hyperbolic 1D tori in the full phase space. Their projection onto the action coordinates is called resonance center line [71] and fulfills

$$s_1 \frac{\partial H_0(\boldsymbol{I})}{\partial I_1} + s_2 \frac{\partial H_0(\boldsymbol{I})}{\partial I_2} = 0. \tag{3}$$

The families of the elliptic and hyperbolic 1D tori build up the skeleton of the resonance channel [72]. The regular structures form a tilted tube in phase space as shown in Fig. 1. Note that the geometry of the 4D normal form system, represented in the section with $\theta_2 = 0$, is very similar to that of a corresponding 4D symplectic map, represented in a 3D phase space slice [73].

The quantum system is obtained from the classical Hamiltonian Eq. (1) by means of Weyl quantization [74], which yields the operators $\hat{\boldsymbol{\theta}}$ and $\hat{\boldsymbol{I}}$ as well as the Hamiltonian $\hat{H} = H_0(\hat{\boldsymbol{I}}) + V(\hat{\boldsymbol{\theta}})$. The eigenvalue equation

$$\hat{H}\,|\psi_{\boldsymbol{m}}\rangle = E\,|\psi_{\boldsymbol{m}}\rangle \tag{4}$$

gives the eigenstates and eigenenergies of the system.

The periodicity of $V(\hat{\boldsymbol{\theta}})$ implies, analogously to Bloch's theorem [75], the discretization of action space, in terms of the grid

$$\boldsymbol{I}_{\boldsymbol{m}} = \hbar(\boldsymbol{m} + \boldsymbol{\vartheta}) \quad \text{with} \quad \boldsymbol{m} \in \mathbb{Z}^2. \tag{5}$$

Here, $\hbar$ denotes an effective Planck's constant, which may be defined as the ratio of Planck's constant and a typical

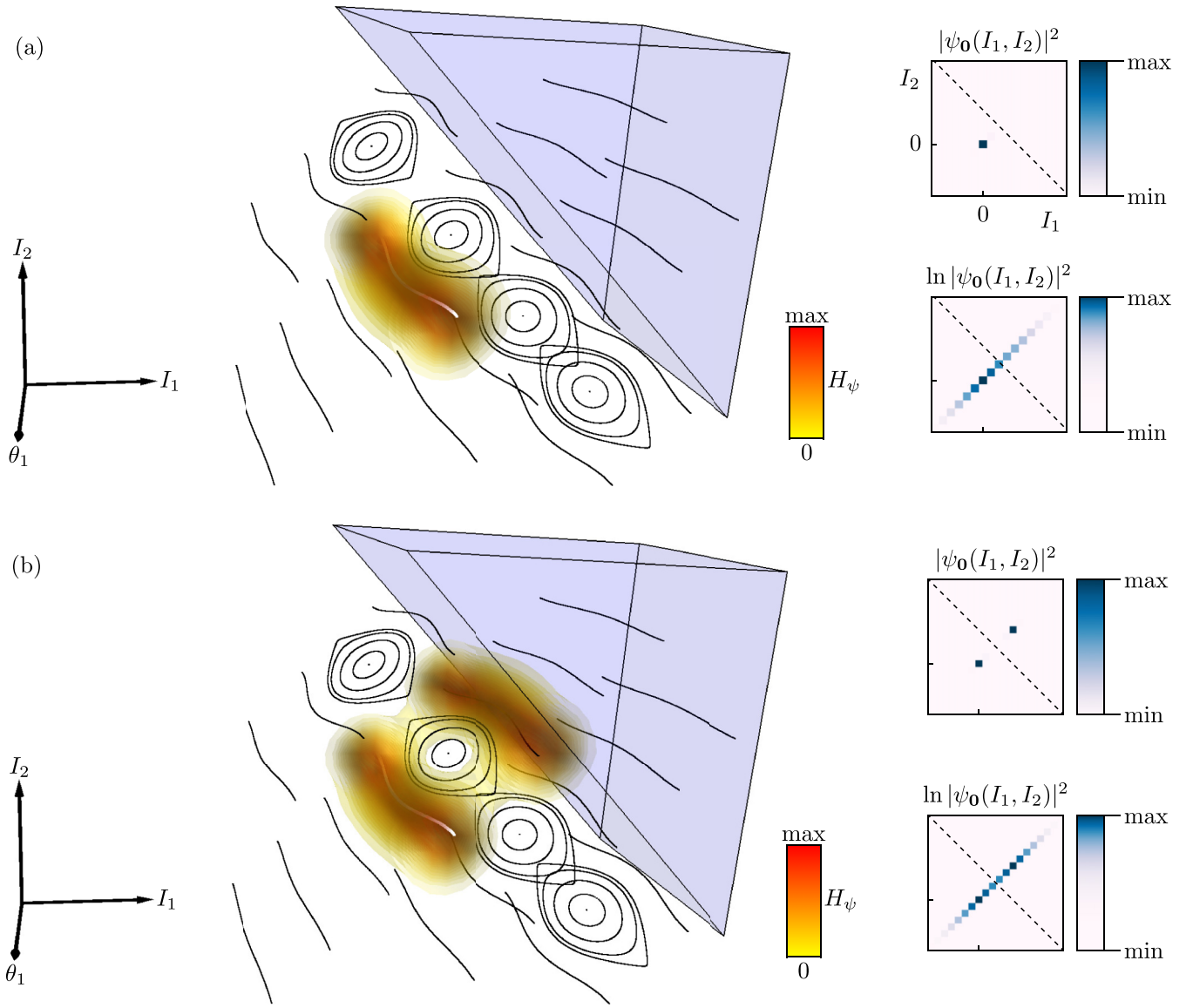

FIG. 1. Phase space of the single coupled resonance shown in a 3D hyperplane for $\theta_2 = 0$ fixed. Regular structures are shown as 1D black curves for four planes with constant polyad number. The eigenstate $|\psi_{\mathbf{0}}\rangle$ maximally localizing on the classical quantizing torus $\boldsymbol{I}_{\mathbf{0}} = (0, 0)$ (white line) is shown in a 3D Husimi phase-space representation (normal scale, see color bar) (a) for $1/h = 0.3450$ and (b) for $1/h = 0.3979$. The region Λ, Eq. (9), trivially extended in the θ_1 direction, is shown in light blue. For comparison, the squared amplitude of the eigenstate $|\psi_{\mathbf{0}}(I_1, I_2)|^2$ is shown in action-space representation (normal and logarithmic scale). The resonance center line, Eq. (3), is shown as dashed line.

action of the system and plays the role of a semiclassical parameter; i.e., $\hbar \to 0$ corresponds to the semiclassical limit. Note that changing the inverse effective Planck constant is experimentally possible, e.g., in a microwave cavity, by varying the frequency [29]. Furthermore, we fix the Bloch phase $\boldsymbol{\vartheta} = (0, 0)$. Evaluation of the Hamiltonian in the action basis Eq. (5) gives the matrix elements

$$\hat{H}_{\boldsymbol{m},\boldsymbol{n}} = H_0(\boldsymbol{I}_{\boldsymbol{n}})\delta_{\boldsymbol{m},\boldsymbol{n}} + V_s(\delta_{\boldsymbol{m},\boldsymbol{n}+s} + \delta_{\boldsymbol{m},\boldsymbol{n}-s}). \tag{6}$$

As we are interested in quantum states in the vicinity of the resonance channel near $\boldsymbol{I} = (0, 0)$, we restrict the action grid to a rectangle, outside which the wave functions are supposed to carry negligible probability. Truncation at $|I_1|, |I_2| \leqslant 10$ gives rise to a finite-dimensional Hilbert space.

Note that $H_0(\hat{\boldsymbol{I}})$ is diagonal in action space and therefore its eigenstates $|\boldsymbol{I}_{\boldsymbol{m}}\rangle$ are labeled by the quantum number $\boldsymbol{m} \in \mathbb{Z}^2$. By means of semiclassical Einstein-Brillouin-Keller (EBK) quantization, this relates them to the quantizing torus $\boldsymbol{I}_{\boldsymbol{m}}$, Eq. (5), of the classical system given by $H_0(\boldsymbol{I})$. As long as $V(\hat{\boldsymbol{\theta}})$ is a small perturbation of $H_0(\hat{\boldsymbol{I}})$, this association of quantum numbers remains valid and the eigenstates of interest localize on quantizing tori of the perturbed Hamiltonian with the same action as $\boldsymbol{I}_{\boldsymbol{m}}$. Our choice of $\boldsymbol{\vartheta} = (0, 0)$ as well as $\boldsymbol{I}_{\text{res}}$, M_{res}, and V_s ensures the existence of an eigenstate $|\psi_{\mathbf{0}}\rangle \equiv |\psi_{\boldsymbol{m}}\rangle$ with quantum number $\boldsymbol{m} = (0, 0)$ which localizes on the corresponding quantizing torus $\boldsymbol{I}_{\mathbf{0}} = (0, 0)$ close to, but still outside of, the resonance channel. In Fig. 1, this torus is depicted as a white line. The choice $\boldsymbol{m} = (0, 0)$ is convenient as it allows us

to study quantum states associated with the same torus when varying $\hbar$.

In order to visualize the eigenstates $|\psi\rangle$ in phase space, we use the Husimi representation [76]

$$H_\psi(\boldsymbol{\theta},\boldsymbol{I}) = \frac{1}{\hbar^2}|\langle\alpha_{\rm coh}(\boldsymbol{\theta},\boldsymbol{I})|\psi\rangle|^2, \tag{7}$$

defined by the overlap of $|\psi\rangle$ with a coherent state $|\alpha_{\rm coh}(\boldsymbol{\theta},\boldsymbol{I})\rangle$ of minimal uncertainty centered at $(\boldsymbol{\theta},\boldsymbol{I})$ given in action representation as

$$\langle\boldsymbol{I}|\alpha_{\rm coh}(\boldsymbol{\theta}_0,\boldsymbol{I}_0)\rangle = \frac{1}{\sqrt{\pi\hbar}}\exp\left[-\frac{(\boldsymbol{I}-\boldsymbol{I}_0)^2}{2\hbar}+\frac{i}{\hbar}\boldsymbol{I}\boldsymbol{\theta}_0\right], \tag{8}$$

and considered on the torus [77].

By fixing $\theta_2 = 0$, the Husimi representation can be compared with the classical phase space structures. Note that this representation is similar to the 3D Husimi representation on the 3D phase space slice [73]. In Fig. 1(a), the eigenstate $|\psi_{\boldsymbol{0}}\rangle$ for $1/h = 0.3450$ is shown. The Husimi representation is localizing on the quantizing torus $\boldsymbol{I_0}$. This can also be seen in the action-space representation as one point with high intensity in the normal scale and exponential tails along a diagonal in action space, as can be seen in the logarithmic scale.

The effect of resonance-assisted tunneling can be measured in various ways. Following the studies of regular-to-chaotic tunneling or partially open quantum systems, we measure the weight of $|\psi_{\boldsymbol{0}}\rangle$ on the opposite side of the resonance $\boldsymbol{s} = (s_1, s_2)$, accounting for the geometry of phase space [48]. In order to determine this weight, we formally follow Ref. [48] and introduce a region Λ in action space given by

$$\begin{aligned}\Lambda := \{(I_1, I_2) \in \mathbb{R}^2 :\\ I_2 \geqslant -\frac{s_1}{s_2}\left(I_1 - I_{\rm res,1}\right) + I_{\rm res,2} + \Lambda_1\}.\end{aligned} \tag{9}$$

The trivial extension of Λ in the θ_1 direction is shown as blue shaded region in Fig. 1. The boundary is chosen parallel to the resonance center line. It is located on the opposite side of the resonance channel with respect to the quantizing torus $\boldsymbol{I_0} = (0, 0)$. Its distance from the resonance channel is controlled by Λ_1. As Λ is dynamically separated from the quantizing torus $\boldsymbol{I_0}$, the weight of the state $|\psi_{\boldsymbol{0}}\rangle$ on Λ measures the strength of tunneling over the resonance channel. For the quantum system, this translates into the projector [48]

$$\hat{P}_\Lambda\,|\boldsymbol{I}\rangle = \chi_\Lambda(\boldsymbol{I})\,|\boldsymbol{I}\rangle\,, \tag{10}$$

where χ_Λ denotes the characteristic function,

$$\chi_\Lambda(\boldsymbol{I}) = \begin{cases}1 & \text{for } \boldsymbol{I} \in \Lambda\\ 0 & \text{for } \boldsymbol{I} \notin \Lambda.\end{cases} \tag{11}$$

The weight $w_{\boldsymbol{0}}$ of $|\psi_{\boldsymbol{0}}\rangle$ in Λ is determined by

$$w_{\boldsymbol{0}} = \|\hat{P}_\Lambda\,|\psi_{\boldsymbol{0}}\rangle\|^2. \tag{12}$$

Note that opening the system in Λ leads to decay rates showing qualitatively the same results as the weights $w_{\boldsymbol{0}}$ [48]. In experiments, the weight can be related to quality factors of optical modes in microcavities or to decay rates of resonance states.

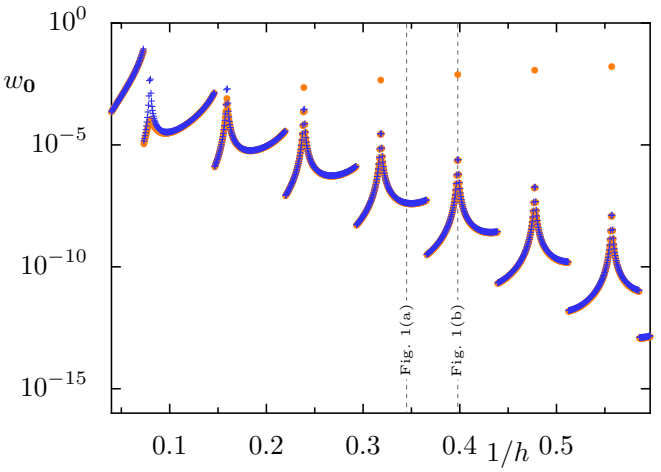

FIG. 2. Weight $w_{\boldsymbol{0}}$ of state $|\psi_{\boldsymbol{0}}\rangle$, see Eq. (12), as function of the inverse effective Planck constant $1/h$ for the single coupled resonance shown as orange bullets. The perturbative prediction (18) is shown as blue crosses.

In Fig. 2, the weight $w_{\boldsymbol{0}}$ is depicted semilogarithmically as a function of the inverse effective Planck constant $1/h$ as orange bullets. On average, it shows an exponential decay with increasing $1/h$, i.e., when approaching the semiclassical limit $\hbar \to 0$. This overall trend is well known from 2D quantum maps [28,44] and experiments [29]. In addition to the overall exponential decay, there are quantization jumps at equidistant values of $1/h$. They are due to points of the discrete action grid that pass the border of the region Λ when h is varied. That is, the quantization jumps are caused by the choice of Λ and the associated projector. In principle, the jumps could be avoided by smoothing the border of the region Λ. However, as these quantization jumps are not related to tunneling, we keep the definition of the projector Eq. (10} for simplicity. In the numerical computation, we choose $\Lambda_1 = 2.35$, which ensures that quantization jumps and peaks do not coincide in the considered range of $1/h$.

Most importantly, on top of the overall exponential decay, there are also sharp peaks occurring in a regular manner at which tunneling is drastically enhanced by several orders of magnitude. These peaks are the manifestation of resonance-assisted tunneling first discussed in 2D systems [27,28]. There, the enhancement of tunneling was traced back to degenerate eigenstates of the unperturbed Hamiltonian, localizing on quantizing tori symmetrically located with respect to the resonance channel. Therefore, also for the 4D system, right on top of one of the peaks, the state $|\psi_{\boldsymbol{0}}\rangle$ is expected to localize equally on the torus $\boldsymbol{I_0}$ and its symmetric counterpart in the plane of the same polyad number. This is nicely seen in the Husimi distribution of $|\psi_{\boldsymbol{0}}\rangle$ for $1/h = 0.3979$ and $\theta_2 = 0$ fixed and the corresponding action-space representation shown in Fig. 1(b). In contrast, away from the peak, the symmetric partner does not belong to the discrete action grid.

In order to gain insight into the underlying mechanism of resonance-assisted tunneling in 4D normal-form systems, we follow Refs. [27,28] and use a perturbative approach to give a quantitative accurate description of the weights. To this

end, we start with $H_0(\hat{\boldsymbol{I}})$ and the orthonormal basis of action states $|\boldsymbol{I}_m\rangle$, in which $H_0(\hat{\boldsymbol{I}})$ is diagonal, and consider $V(\hat{\boldsymbol{\theta}})$ as a sufficiently small perturbation. The only nonvanishing matrix elements of $V(\hat{\boldsymbol{\theta}})$ occur between action states whose quantum numbers differ by $\pm\boldsymbol{s}$:

$$\langle \boldsymbol{I}_m | \, V(\hat{\boldsymbol{\theta}}) \, | \boldsymbol{I}_{m+s} \rangle = V_s. \tag{13}$$

The perturbative expansion of a state localizing predominantly on the quantizing torus $\boldsymbol{I}_m$ is thus given by [9,10]

$$\left| \psi_m^{\text{pert}} \right\rangle = |\boldsymbol{I}_m\rangle + \sum_{l \in \mathbb{Z}\setminus\{0\}} A_m^{(l)} \, |\boldsymbol{I}_{m+ls}\rangle \, . \tag{14}$$

As the polyad number has a quantum mechanical analog given by the polyad number operator $\hat{n} = s_2\hat{I}_1 - s_1\hat{I}_2$ commuting with $\hat{H}$, only states within the subspace of same polyad number contribute to this perturbative expansion. For fixed l, the coefficient $A_m^{(l)}$ can be decomposed into distinct contributions λ_m^Γ that differ in the order of perturbation theory. Each contribution is uniquely associated with a sequence $\Gamma = [\boldsymbol{t}_1, \boldsymbol{t}_2, \ldots, \boldsymbol{t}_k]$ of couplings with $\boldsymbol{t}_i \in \{\pm\boldsymbol{s}\}$ which defines a path on the action grid. The length of the path is given by the number of elements in the sequence and is denoted as $|\Gamma| := k$. It coincides with the order of perturbation theory in which Γ contributes.

A path can contribute to $A_m^{(l)}$ only if $|\Gamma| \geqslant |l|$. Graphically such a path Γ connects $\boldsymbol{I}_m$ with $\boldsymbol{I}_{m+ls}$ on the discrete action grid, where intermediate subsequent actions differ by $\pm\boldsymbol{s}$ in their quantum numbers.

Schematically this is illustrated in Fig. 3, where the action grid is indicated by gray points and the region Λ is shaded blue. Figure 3(a) shows the path $\Gamma = [\boldsymbol{s}, \boldsymbol{s}]$ of length $|\Gamma| = 2$ connecting $\boldsymbol{I}_\mathbf{0}$, marked as green point, with $\boldsymbol{I}_{(2,2)}$. In Fig. 3(b), the path $\Gamma = [\boldsymbol{s}, \boldsymbol{s}, \boldsymbol{s}]$ of length $|\Gamma| = 3$ ending on $\boldsymbol{I}_{(3,3)}$ is shown.

Let $\mathcal{M}_m^l$ denote the set of all paths which connect $\boldsymbol{I}_m$ with $\boldsymbol{I}_{m+ls}$ and for which no intermediate action coincides with $\boldsymbol{I}_m$, i.e., paths coming back to their starting point are excluded in the following according to perturbation theory [78]. Each path $\Gamma \in \mathcal{M}_m^l$ then contributes with

$$\lambda_m^\Gamma = V_s^{|\Gamma|} \prod_{i=1}^{|\Gamma|} \frac{1}{H_0(\boldsymbol{I}_m) - H_0\left(\boldsymbol{I}_{m+\sum_{j=1}^{i} \boldsymbol{t}_j}\right)}, \tag{15}$$

which includes the unperturbed energies of the intermediate actions. Finally, the contributions from different paths add up to the coefficients

$$A_m^{(l)} = \sum_{\Gamma \in \mathcal{M}_m^l} \lambda_m^\Gamma. \tag{16}$$

Inserting the state $|\psi_m^{\text{pert}}\rangle$, Eq. (14), into Eq. (12), we find for the weight in the region Λ

$$w_m = \sum_{\substack{l \in \mathbb{N} \\ \boldsymbol{I}_{m+ls} \in \Lambda}} \left| A_m^{(l)} \right|^2. \tag{17}$$

From the 2D case, it is known that it suffices to take only the unique shortest path $\Gamma_l = [\boldsymbol{s}, \boldsymbol{s}, \ldots \boldsymbol{s}]$ of length l into account. The sum in Eq. (17) may thus be rewritten as a sum over all positive integers l starting from the smallest integer $l_{\min}$ for which $\boldsymbol{I}_{m+l_{\min}\boldsymbol{s}} \in \Lambda$ holds and where we approximate $A_m^{(l)} \approx \lambda_m^{\Gamma_l}$. In particular, neglecting all but the lowest contributing order $l_{\min}$ of perturbation theory, i.e., including only the shortest path, Eq. (17) reduces to

$$w_m = \left| \lambda_m^{\Gamma_{l_{\min}}} \right|^2. \tag{18}$$

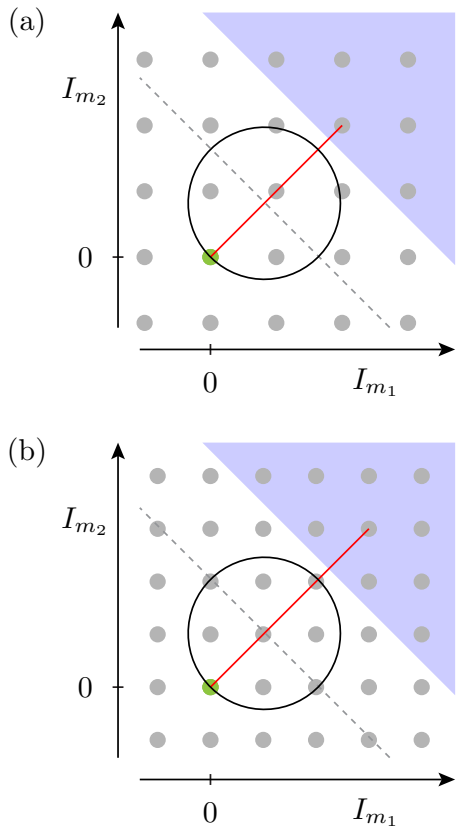

FIG. 3. Scheme of perturbation theory for the single coupled resonance. The action grid $\boldsymbol{I}_m$ is depicted as gray points, the quantizing torus $\boldsymbol{I}_\mathbf{0} = (0, 0)$ as green point. The dashed line shows the position of the resonance center line; see Eq. (3). The circle indicates the level set of constant energy $H_0(\boldsymbol{I}_\mathbf{0})$. The blue shaded area shows the region Λ; see Eq. (9). The red line indicates the shortest path Γ. (a) The nonresonant case for $1/h = 0.1314$ and $|\Gamma| = 2$. (b) The resonant case for $1/h = 0.1638$ and $|\Gamma| = 3$.

Note that the paths shown in Fig. 3 are exactly the shortest for the two different values of $1/h$, respectively. This lowest order approximation already leads to excellent agreement with the weights $w_\mathbf{0}$ obtained from diagonalization of the Hamiltonian, see Fig. 2, where the prediction Eq. (18) is shown as blue crosses comparing very well with the numerical results. This is because higher orders are suppressed by $|V_s|$, i.e., by at least one order of magnitude.

The emergence of resonance-assisted tunneling peaks can be traced back to the energy denominators in Eq. (15). The contribution λ_m^Γ diverges whenever intermediate states $|\boldsymbol{I}_{m+ls}\rangle$ and $|\boldsymbol{I}_m\rangle$ are resonant; i.e., they are energetically degenerate with respect to $H_0(\hat{\boldsymbol{I}})$, which gives rise to the peaks. This mechanism is well known from 2D systems. It is further illustrated in Fig. 3(a), where the nonresonant case is shown. There no intermediate state lies on the circular level set

of constant energy $H_0(\boldsymbol{I}) = H_0(\boldsymbol{I_0}) =$ constant. In contrast, Fig. 3(b) depicts the resonant case where both $\boldsymbol{I_0}$ and $\boldsymbol{I}_{(2,2)}$ have approximately the same unperturbed energy. Note that in the case of exact degeneracy of $\boldsymbol{I_0}$ with an intermediate state, the perturbative prediction diverges and thus looses its validity. This situation, which in principle could be treated by degenerate perturbation theory, is also ignored in the work on the 2D system. Furthermore, quantization jumps occur in the perturbative result as well and coincide with the values of $1/h$ at which the length $l_{\min}$ of the shortest path into the region Λ changes by one. Despite being a 4D system due to integrability and both classically and quantum mechanically conserved polyad number $s_2 I_1 - s_1 I_2$, the results closely resemble what is known from 2D systems.

B. Double resonance

Resonances of higher rank are possible in higher dimensional systems only. The minimal example is the double resonance in a 4D system. Using normal-form theory and truncation yields an effective Hamiltonian [56–60]

$$H(\boldsymbol{\theta}, \boldsymbol{I}) = H_0(\boldsymbol{I}) + 2V_{\boldsymbol{r}} \cos(\boldsymbol{r\theta}) + 2V_{\boldsymbol{s}} \cos(\boldsymbol{s\theta}), \tag{19}$$

which describes the dynamics in the vicinity of a double resonance, occurring at the isolated minimum of $H_0(\boldsymbol{I})$. When we use Eq. (2) for $H_0(\boldsymbol{I})$, this minimum occurs at $\boldsymbol{I} = \boldsymbol{I}_{\text{res}}$. Choosing linear independent resonance vectors $\boldsymbol{r}, \boldsymbol{s}$ gives rise to two different resonance channels parametrized by the corresponding resonance center line; see Eq. (3). At the intersection of both resonance center lines, i.e., the minimum of $H_0(\boldsymbol{I})$, the double resonance condition is fulfilled.

In general, Eq. (19) gives rise to nonintegrable dynamics, except for specific choices of $\boldsymbol{r}, \boldsymbol{s}$ [60]. In particular, due to the second resonant term, the polyad numbers corresponding to either of the two resonance vectors are no longer conserved. However, whenever perturbations are small, the system still can be considered as near integrable.

In the following, we choose $\boldsymbol{r} = (r_1, r_2) = (1, 0)$ and $\boldsymbol{s} = (s_1, s_2) = (1, 1)$ as linearly independent resonance vectors with prefactors $V_{\boldsymbol{r}} = V_{\boldsymbol{s}} = 0.05$ and $H_0(\boldsymbol{I})$ as given by Eq. (2) for $M_{\text{res}} = 1$ and $\boldsymbol{I}_{\text{res}} = (1.0, 1.0)$. The phase space is shown in the 3D hyperplane for fixed $\theta_2 = 0$ in Fig. 4. Both resonance vectors give rise to a resonance channel intersecting in a so-called resonance junction at the minimum of $H_0(\boldsymbol{I})$ at $\boldsymbol{I}_{\text{res}} = (1.0, 1.0)$. This corresponds to the point in which the double resonance condition is fulfilled. It gives rise to four equilibria with different types of stability, namely one elliptic-elliptic at $(\theta_1, \theta_2) = (\pi, 0)$, one hyperbolic-hyperbolic at $(0, 0)$, and and two elliptic-hyperbolic at $(0, \pi)$ and (π, π) respectively [79,80]. Together with their invariant manifolds or attached families of elliptic 1D tori, they organize the phase space close to $\boldsymbol{I}_{\text{res}}$. Along the resonance center line of each resonance and sufficiently far away from $\boldsymbol{I}_{\text{res}}$, the phase space locally resembles the phase space of a 2D pendulum and is governed by the associated resonance channel. Following the resonance channels toward the junction at $\boldsymbol{I}_{\text{res}}$ chaotic layers of both resonance channels begin to overlap and form a connected stochastic layer. As usual in nonintegrable systems, also resonances of higher order occur. These regular resonance structures are not shown but are indirectly seen by the small holes in the chaotic layers.

From Fig. 4, we conclude that phase space and action space are each divided into four dynamically separated regions by the resonance channels and the resonance center lines, respectively. Therefore, tunneling across both of the resonance channels is expected. As the chaotic layer does not support a relevant number of chaotic eigenstates in the considered regime of $\hbar$, we do not expect it to influence tunneling.

Accounting for the additional second resonant term in Eq. (19), the matrix elements of the quantized Hamiltonian read

$$\begin{aligned}\hat{H}_{\boldsymbol{m},\boldsymbol{n}} = H_0(\boldsymbol{I_n})\delta_{\boldsymbol{m},\boldsymbol{n}} &+ V_{\boldsymbol{s}}(\delta_{\boldsymbol{m},\boldsymbol{n}+\boldsymbol{s}} + \delta_{\boldsymbol{m},\boldsymbol{n}-\boldsymbol{s}}) \\ &+ V_{\boldsymbol{r}}(\delta_{\boldsymbol{m},\boldsymbol{n}+\boldsymbol{r}} + \delta_{\boldsymbol{m},\boldsymbol{n}-\boldsymbol{r}}).\end{aligned} \tag{20}$$

Our choice of parameters guarantees the existence of a quantizing torus $\boldsymbol{I_0}$ for all values of the effective Planck's constant. This allows for studying tunneling of the eigenstate $|\psi_{\boldsymbol{0}}\rangle$ in terms of its weight in a properly chosen region Λ in action space located on opposite sides of both resonance channels. We choose

$$\begin{aligned}\Lambda := \big\{(I_1, I_2) \in \mathbb{R}^2 :\ & \\ I_2 \geqslant -\frac{s_1}{s_2}(I_1 - I_{\text{res},1}) + I_{\text{res},2} + \Lambda_1,& \\ I_1 \geqslant \Lambda_2\big\}.&\end{aligned} \tag{21}$$

For numerical computations, we set $\Lambda_1 = 1.7$ and $\Lambda_2 = 2.7$. In Fig. 4, the region Λ is shown as a light blue region, trivially extended in the θ_1 direction. Using Λ in the definition of the projector Eq. (10), the weight $w_{\boldsymbol{0}}$ is again given by Eq. (12).

The weight $w_{\boldsymbol{0}}$ of $|\psi_{\boldsymbol{0}}\rangle$ on Λ is shown in Fig. 5 as a function of the inverse effective Planck constant $1/h$ by orange bullets. Besides the overall exponential decay of the weight in the region Λ, various peaks are visible, e.g., as indicated by the vertical dashed lines at $1/h = 0.1591$ and $1/h = 0.1991$. These peaks occur in a very complicated manner and have a strong variation of their widths. Furthermore, between the peaks also a drastic decrease of the weight $w_{\boldsymbol{0}}$ is observed, e.g., for $1/h \approx 0.146$. Apart from peaks and suppression, also plateaus of nearly constant weight over some interval of $1/h$ are present, for example, around the vertical dashed line at $1/h = 0.375$.

In Fig. 4, Husimi representations and the corresponding action-space representations in normal and logarithmic scale of $|\psi_{\boldsymbol{0}}\rangle$ are shown for different values of $1/h$. For the nonresonant case at $1/h = 0.375$, see Fig. 4(a), the state $|\psi_{\boldsymbol{0}}\rangle$ localizes mainly on the quantizing torus $\boldsymbol{I_0}$ (white line). The Husimi representations for $1/h = 0.1991$ and $1/h = 0.1591$ in Figs. 4(b) and 4(c) show resonant eigenstates with a significant weight in dynamically distinct regions. Both cross the resonance junction; however, the morphology of the states differs, best seen in the action-space representation, which can be explained in terms of perturbation theory, which is discussed next.

In order to explain the underlying mechanism of resonance-assisted tunneling in the case of a double resonance, we use a perturbative approach. As in Sec. II A, we

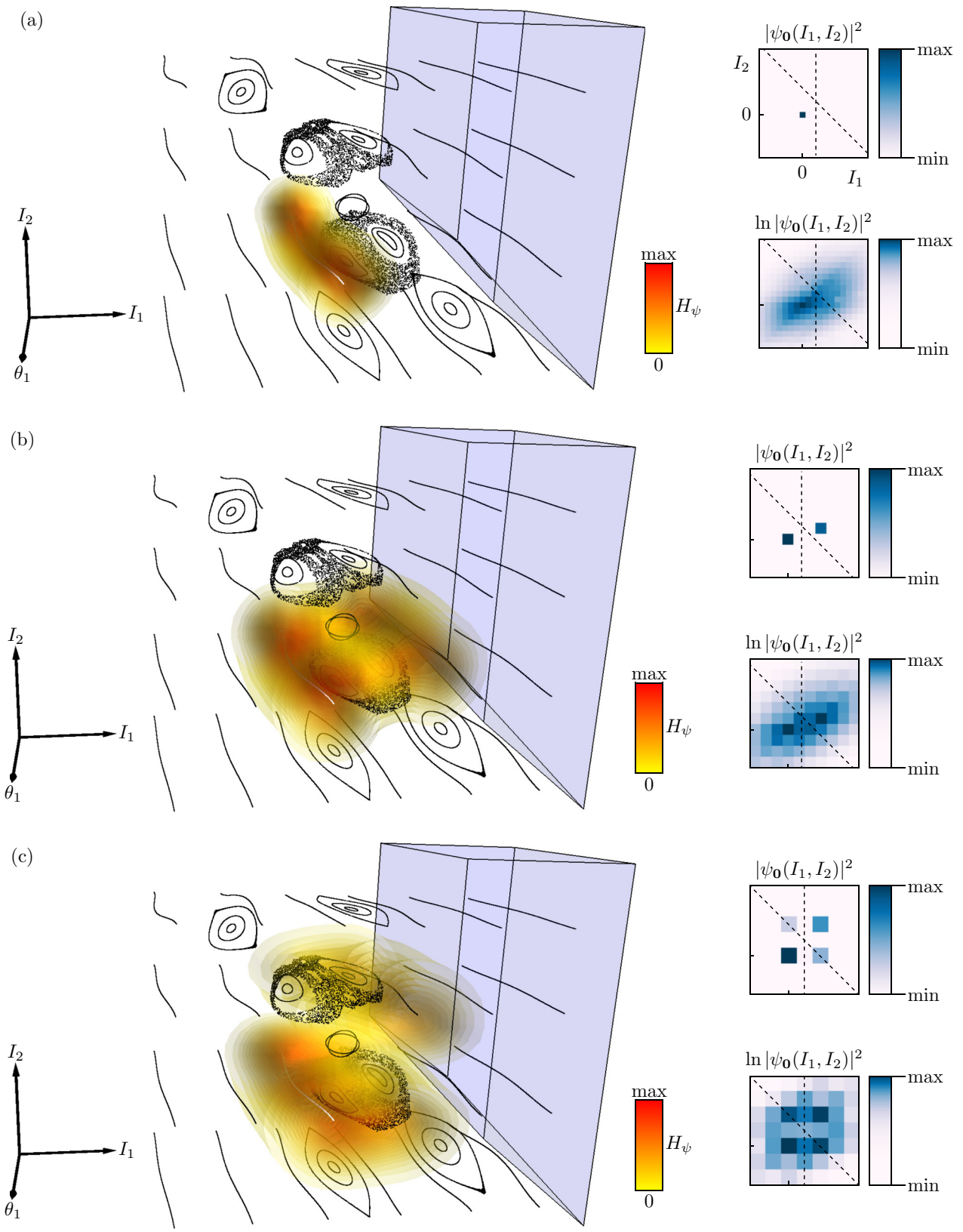

FIG. 4. Phase space of the double resonance shown in a 3D hyperplane for $\theta_2 = 0$ fixed. Regular structures are shown as 1D black curves, whereas chaotic structures are shown as points. The eigenstate $|\psi_{\mathbf{0}}\rangle$ maximally localizing on the classical quantizing torus $\boldsymbol{I}_{\mathbf{0}} = (0, 0)$ (white line) is shown in a 3D Husimi phase-space representation (normal scale, see color bar) (a) for $1/h = 0.375$, (b) for $1/h = 0.1991$, and (c) for $1/h = 0.1591$. The region Λ, Eq. (21), trivially extended in the θ_1 direction, is shown in light blue. For comparison, the squared amplitude of the eigenstate $|\psi_{\mathbf{0}}(I_1, I_2)|^2$ is shown in action-space representation (normal and logarithmic scale). The resonance center lines, Eq. (3), are shown as dashed lines.

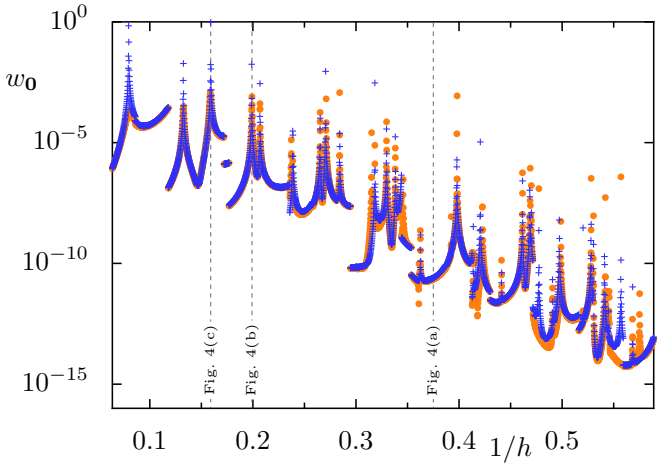

FIG. 5. Weight $w_{\mathbf{0}}$ of state $|\psi_{\mathbf{0}}\rangle$, see Eq. (12), as function of the inverse effective Planck constant $1/h$ for the double resonance is shown as orange bullets. The perturbative prediction (27), only using the shortest paths, is shown as blue crosses.

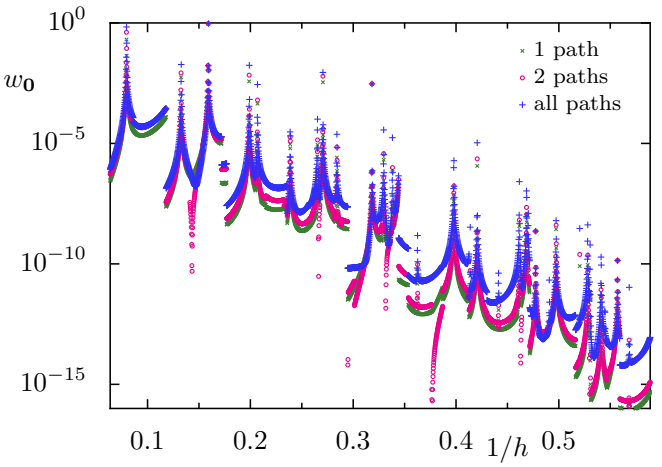

FIG. 6. Perturbative prediction using Eq. (27) incorporating an increasing number of paths sorted by the absolute value of their contribution $|\lambda_{\boldsymbol{m}}^{\Gamma}|$. Prediction for one path is shown as crosses, for two paths as circles, and for all paths as squares.

start with the unperturbed system but also consider the second resonant term allowing for two nonvanishing matrix elements

$$\langle \boldsymbol{I_m}| V(\hat{\boldsymbol{\theta}}) |\boldsymbol{I_{m+r}}\rangle = V_{\boldsymbol{r}}, \tag{22}$$

$$\langle \boldsymbol{I_m}| V(\hat{\boldsymbol{\theta}}) |\boldsymbol{I_{m+s}}\rangle = V_{\boldsymbol{s}}, \tag{23}$$

for quantum numbers differing by $\pm\boldsymbol{s}$ and $\pm\boldsymbol{r}$. The perturbative expansion developed in Ref. [78] and previously similarly applied to resonance-assisted tunneling in the 2D case with multiple rank-1 resonances [9,81] reads

$$\left|\psi_{\boldsymbol{m}}^{\text{pert}}\right\rangle = |\boldsymbol{I_m}\rangle + \sum_{(k,l)\in\mathbb{Z}^2\setminus\{\mathbf{0}\}} A_{\boldsymbol{m}}^{(k,l)} |\boldsymbol{I_{m+kr+ls}}\rangle \tag{24}$$

for the state localizing predominantly on the quantizing torus $\boldsymbol{I_m}$. As Eqs. (22) and (23) suggest, there are twice the number of possibilities of subsequent couplings in each order of perturbation theory compared to the case of the single resonance. Thus, in the perturbative expansion of $|\psi_{\boldsymbol{m}}^{\text{pert}}\rangle$, an unperturbed state $|\boldsymbol{I_{m+kr+ls}}\rangle$ contributes with a coefficient obtained by all paths Γ which connect the initial quantizing torus $\boldsymbol{I_m}$ with the final torus $\boldsymbol{I_{m+kr+ls}}$ in the discrete action grid, where subsequent actions differ in their quantum numbers by $\pm\boldsymbol{r}$ or $\pm\boldsymbol{s}$, respectively. Let $\mathcal{M}_{\boldsymbol{m}}^{k,l}$ be the set of these paths. In contrast to Sec. II A, here every path $\Gamma \in \mathcal{M}_{\boldsymbol{m}}^{k,l}$ corresponds to a sequence $\Gamma = [\boldsymbol{t}_1, \boldsymbol{t}_2, \ldots, \boldsymbol{t}_{|\Gamma|}]$ with $\boldsymbol{t}_i \in \{\pm\boldsymbol{r}, \pm\boldsymbol{s}\}$. Again, paths which return to $\boldsymbol{I_m}$ at some point are excluded from $\mathcal{M}_{\boldsymbol{m}}^{k,l}$. Taking all paths into account, the coefficients in Eq. (24) read

$$A_{\boldsymbol{m}}^{(k,l)} = \sum_{\Gamma\in\mathcal{M}_{\boldsymbol{m}}^{k,l}} \lambda_{\boldsymbol{m}}^{\Gamma} \tag{25}$$

and every path contributes with

$$\lambda_{\boldsymbol{m}}^{\Gamma} = \prod_{i=1}^{|\Gamma|} \frac{V_{\boldsymbol{t}_i}}{H_0(\boldsymbol{I_m}) - H_0\left(\boldsymbol{I}_{\boldsymbol{m}+\sum_{j=1}^{i}\boldsymbol{t}_j}\right)}, \tag{26}$$

where we define $V_{-\boldsymbol{t}} = V_{\boldsymbol{t}}$ for $\boldsymbol{t} \in \{\pm\boldsymbol{r}, \pm\boldsymbol{s}\}$.

Inserting the obtained state $|\psi_{\boldsymbol{m}}^{\text{pert}}\rangle$ of Eq. (24) into Eq. (12), and using the definition of the projection operator $\hat{P}_{\Lambda}$, see Eq. (10), we find

$$w_{\boldsymbol{m}} = \sum_{\substack{(k,l)\in\mathbb{Z}^2 \\ \boldsymbol{I}_{\boldsymbol{m}+k\boldsymbol{r}+l\boldsymbol{s}}\in\Lambda}} \left|A_{\boldsymbol{m}}^{(k,l)}\right|^2. \tag{27}$$

In order to apply Eq. (27), we consider only the shortest paths Γ, which reach Λ as they give rise to the lowest order contributions. Let n be the length of these paths. For our choice of the resonance vectors $\boldsymbol{r}$ and $\boldsymbol{s}$, this restricts the relevant endpoints $\boldsymbol{I}_{\boldsymbol{m}+k\boldsymbol{r}+l\boldsymbol{s}}$ to those where $k+l=n$ for positive k and l. Given $(k,l) \in \mathbb{N}^2$ the set $\mathcal{M}_{\boldsymbol{m}}^{k,l}$ then contains $\binom{n}{l}$ of these shortest paths. Here, taking only the shortest paths into account, i.e., the lowest order of perturbation theory, gives excellent agreement with the weights obtained from numerical diagonalization. This can be seen in Fig. 5 where the perturbative prediction of $w_{\mathbf{0}}$, Eq. (27), shown as blue crosses, is compared with the numerically obtained weights. The perturbative description covers the overall exponential decay as well as the peaks and plateaus. Note that, in general, considering only the shortest paths may not be sufficient. One such example is the peak near $1/h = 0.5751$. As in the case of the single resonance, the peaks arise whenever an intermediate state along one or more perturbative paths is resonant with $\boldsymbol{I_m}$. Furthermore, quantization jumps occur when the minimal length of paths, which reach Λ, increases by one.

In contrast to the single resonance case, there is a larger number of shortest paths which enter the prediction Eq. (27). As all these paths have the same length, it is *a priori* not clear which of them will give the dominant contribution and which paths need to be taken into account to achieve the accuracy presented in Fig. 5. To this end, we sort all contributing paths by their absolute value $|\lambda_{\boldsymbol{m}}^{\Gamma}|$ in descending order. In Fig. 6, the perturbative result is shown for an increasing number of shortest paths Γ. Using only the path with the greatest absolute value for a given inverse Planck's constant $1/h$ is shown as crosses. While the positions of the peaks are already resolved, the plateau-like structures show a mismatch of several orders of magnitude.

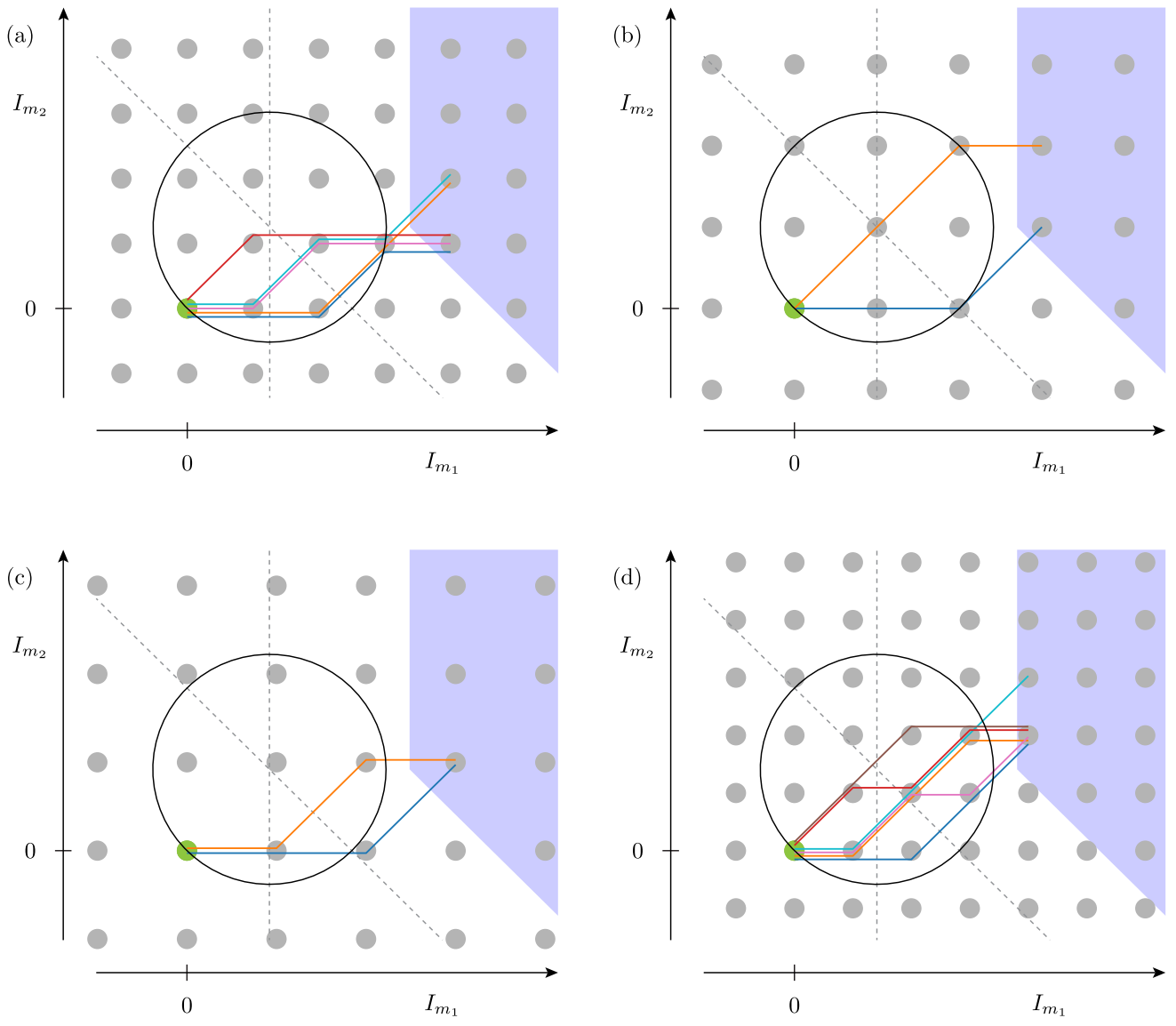

FIG. 7. Scheme of perturbation theory for the double resonance. The action grid $\boldsymbol{I_m}$ is depicted as gray points and the quantizing torus $\boldsymbol{I_0} = (0, 0)$ as green point. The dashed lines show the position of the two resonance center lines; see Eq. (3). The circle indicates the level set of constant energy $H_0(\boldsymbol{I_0})$. The blue shaded area shows the region Λ; see Eq. (21). In panel (a) for $1/h = 0.1991$, five paths with an resonant intermediate state are shown, and in panel (b) for $1/h = 0.1591$, two resonant paths with different intermediate state are shown. In Figs. 4(b) and 4(c), both states are shown in a Husimi representation. In panel (c) for $1/h = 0.1465$, two canceling paths are shown, and in panel (d) for $1/h = 0.2244$, six nonresonant paths are shown.

In general there is not necessarily one single dominating path, but several paths may give rise to similar contributions. This case is illustrated in Fig. 7(a) for $1/h = 0.1991$ where on the action grid five paths containing the resonant intermediate state $\boldsymbol{I}_{(3,1)}$ fulfilling $H_0(\boldsymbol{I_0}) = H_0(\boldsymbol{I}_{(3,1)})$ are shown. All these paths contribute to $w_{\boldsymbol{0}}$ within the same order of magnitude. Thus, considering only the most contributing path resolves the position of the peaks while adding all resonant paths refines the prediction. The sixth most contributing path, however, gives rise to a contribution which is two orders of magnitude smaller since no intermediate state is located on the circular level set of constant energy $H_0(\boldsymbol{I_0})$. Therefore, excluding these nonresonant paths (if other resonant paths exist) does not affect the result.

In Fig. 7(b), two points of the action grid $\boldsymbol{I}_{(2,0)}$ and $\boldsymbol{I}_{(2,2)}$ are close to the level set of energy $H_0(\boldsymbol{I_0})$ for $1/h = 0.1591$. Thus, both paths with a resonant intermediate state are essential for an accurate prediction of the weight. This also nicely explains the different morphologies of the Husimi distributions and action-space representations; see Figs. 4(b) and 4(c). In 4(c), the state $|\psi_{\boldsymbol{0}}\rangle$ has a higher density at the position of both resonant intermediate states $\boldsymbol{I}_{(2,0)}$ and $\boldsymbol{I}_{(2,2)}$. In contrast, in Fig. 4(b) only the intermediate state $\boldsymbol{I}_{(3,1)}$ shows a higher density.

In contrast to the case where several paths with resonant intermediate states constructively interfere, also the case of destructive interference of tunneling paths occurs. This is best seen in the perturbative prediction arising from two

paths depicted in Fig. 6 as circles. For specific values of $1/h$, e.g., around $1/h = 0.1465$, a drastic decrease of $w_{\mathbf{0}}$ can be observed. This happens if the two paths Γ_1 and Γ_2 under consideration fulfill $\lambda_{\boldsymbol{m}}^{\Gamma_1} = -\lambda_{\boldsymbol{m}}^{\Gamma_2}$. Figure 7(c) illustrates this scenario, where two paths cancel each other. The two involved paths differ in their intermediate steps $\boldsymbol{I}_{(2,0)}$ and $\boldsymbol{I}_{(2,1)}$, respectively. These states lie on different sides of the level set of constant energy such that the denominator in Eq. (26) differs in its sign but is of equal absolute value. Taking only the two most contributing paths into account thus gives a qualitative description of the observed suppression of tunneling. Such mechanism is also known from 2D maps if several single resonances are present [9,10]. The basic features, i.e., the overall exponential decay, the peaks, and the suppression of tunneling, are already captured if only two paths are taken into account, whereas considering all shortest paths compensates the effect of destructive interference of paths as depicted in Fig. 6. Furthermore, it emphasizes the necessity to consider all paths for a quantitatively accurate prediction of the plateau-like structures pronounced in the regime of large $1/h$. Schematically, the importance for considering all paths is depicted in Fig. 7(d), showing only the first six most contributing nonresonant paths for $1/h = 0.2244$. By considering all paths, the weight of plateaulike structures can be quantitatively predicted.

Note that for arbitrary resonance vectors, higher orders of perturbation theory may be necessary, for instance, if there are paths with a resonant intermediate state which need an additional step to reach Λ. In other words, the shortest paths do not necessarily lead to the largest contribution. If necessary, these longer paths can be computed easily to refine the prediction. In the considered system, including only the shortest path in the perturbative expression Eq. (27) allows for a successful prediction of the numerically obtained weight $w_{\mathbf{0}}$, see Eq. (12), over several orders of magnitude.

C. A 4 × 4 matrix model

The underlying mechanism of the enhancement and suppression of the weight $w_{\boldsymbol{m}}$ in the situation of a double resonance can be explained within a minimal 4×4 matrix model. To this end, we consider four states $|\boldsymbol{I}_i\rangle$ resembling the unperturbed action states $|\boldsymbol{I}_{\boldsymbol{m}}\rangle$ corresponding to the quantizing actions $\boldsymbol{I}_0 = \boldsymbol{I}_{(0,0)} = (0,0)$, $\boldsymbol{I}_1 = \boldsymbol{I}_{(1,0)} = (\hbar, 0)$, $\boldsymbol{I}_2 = \boldsymbol{I}_{(1,1)} = (\hbar, \hbar)$, and $\boldsymbol{I}_3 = \boldsymbol{I}_{(2,1)} = (2\hbar, \hbar)$. The unperturbed energies of these states are given by $E_i = H_0(\boldsymbol{I}_i)$; see Eq. (2). We allow for couplings between these states according to Eqs. (22) and (23). The matrix representation then reads

$$\hat{H}_{4\times4} = \begin{pmatrix} E_0 & V_{\boldsymbol{r}} & V_{\boldsymbol{s}} & 0 \\ V_{\boldsymbol{r}} & E_1 & 0 & V_{\boldsymbol{s}} \\ V_{\boldsymbol{s}} & 0 & E_2 & V_{\boldsymbol{r}} \\ 0 & V_{\boldsymbol{s}} & V_{\boldsymbol{r}} & E_3 \end{pmatrix}. \tag{28}$$

Diagonalization of $\hat{H}_{4\times4}$ for a fixed value of $\hbar$ yields the eigenstates $|\psi_i\rangle$ in the basis of action eigenstates. We choose for H_0 the parameters $M_{\text{res}} = 1$ and $\boldsymbol{I}_{\text{res}} = (0.35, 0.55)$ and for the resonances $\boldsymbol{r} = (1,0)$ and $\boldsymbol{s} = (1,1)$ with corresponding coupling strengths $V_{\boldsymbol{r}} = 0.0025$ and $V_{\boldsymbol{s}} = 0.005$, respectively. As the perturbations are small, the eigenstates will predominantly resemble one of the action states and are labeled accordingly. Thus, resonance-assisted tunneling between $\boldsymbol{I}_0$ and $\boldsymbol{I}_3$ can be quantified by the overlap

$$w_0 = |\langle\psi_0|\boldsymbol{I}_3\rangle|^2 \tag{29}$$

between the state $|\psi_0\rangle$ associated with $\boldsymbol{I}_0$ and the state $|\boldsymbol{I}_3\rangle$. The states $|\boldsymbol{I}_1\rangle$ and $|\boldsymbol{I}_2\rangle$ deal as intermediate states. In Fig. 8(a), the weight w_0 is depicted as a function of $\hbar$ as (orange) line. It resembles the basic features of resonance-assisted tunneling observed in the full system with a double resonance. In particular, the 4×4 matrix models shows three peaks of enhancement as well as suppression in between the second and third peaks.

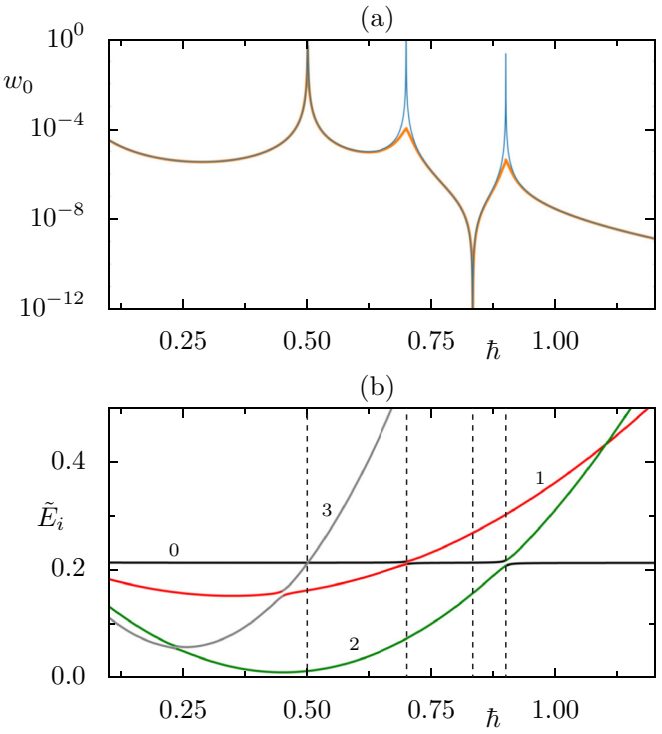

FIG. 8. Matrix model: (a) Weight w_0 as a function of $\hbar$ obtained via Eq. (29) shown as orange line and $w_{0,\text{pert}}$ calculated using Eq. (32) as blue line. (b) Energies $\tilde{E}_i$ (solid lines) of the states $|\psi_i\rangle$ as a function of $\hbar$ in black, red, green, and gray for $i = 0, 1, 2, 3$. The vertical dashed lines indicate the values of $\hbar$ for the cases of enhancement and suppression.

In the following, we treat the 4×4 matrix model also perturbatively. In order to compute the weight w_0, Eq. (29), there are only two paths to be considered. They connect $\boldsymbol{I}_0$ with $\boldsymbol{I}_3$ and differ by their intermediate step. Explicitly, they are given by $\Gamma_1 = [\boldsymbol{r}, \boldsymbol{s}]$ and $\Gamma_2 = [\boldsymbol{s}, \boldsymbol{r}]$ and contribute with

$$\lambda_1 = \frac{V_{\boldsymbol{r}}}{E_0 - E_1}\frac{V_{\boldsymbol{s}}}{E_0 - E_3}, \tag{30}$$

$$\lambda_2 = \frac{V_{\boldsymbol{s}}}{E_0 - E_2}\frac{V_{\boldsymbol{r}}}{E_0 - E_3}. \tag{31}$$

The perturbatively computed weight is given by

$$w_{0,\text{pert}} = |\lambda_1 + \lambda_2|^2 \tag{32}$$

and is shown as the (blue) line in Fig. 8(a). They are in perfect agreement with the numerically obtained weights away from

the peaks and as long as the coupling terms are sufficiently small. The position of the peaks are given by the denominators of Eqs. (30) and (31), whenever there is a degeneracy of the unperturbed state $|\boldsymbol{I}_0\rangle$ with either one of the remaining three states. This is exactly the case for $\hbar = 2I_{\mathrm{res},1}$, $\hbar = I_{\mathrm{res},1} + I_{\mathrm{res},2}$ and $\hbar = \frac{4I_{\mathrm{res},1}+I_{\mathrm{res},2}}{5}$. Instead, destructive interference occurs if $\lambda_1 = -\lambda_2$ which is equivalent to $(E_0 - E_1) = -(E_0 - E_2)$ and holds for $\hbar = \frac{4I_{\mathrm{res},1}+2I_{\mathrm{res},2}}{3}$. The values of $\hbar$ for enhancement and suppression are marked in Fig. 8 as black dashed lines. For the case of suppression, the origin of the opposing signs can be read off from the denominators of Eqs. (30) and (31), indicating that states $\boldsymbol{I}_1$ and $\boldsymbol{I}_2$ lie on different sides of the level set of constant energies and have equal energy difference from E_0 but with a different sign.

Additionally, in Fig. 8(b) the energy levels $\tilde{E}$ of the eigenstates $|\psi_i\rangle$ are shown. The black line corresponds to $\tilde{E}_0$ and shows avoided crossings with either the energies of the intermediate states (green and red) or the energy of the final state (gray). The positions of these avoided crossings match with the positions of the peaks of enhancement of the weight w_0. On the other hand, in the case of suppression, the energy difference between $\tilde{E}_0$ and the energy of the two intermediate states is equal in size, but of opposite sign.

III. SUMMARY AND OUTLOOK

In this paper, we studied resonance-assisted tunneling by exploiting the universal description of the classical dynamics in the vicinity of a nonlinear resonance in terms of normal-form Hamiltonians. In particular, we concentrated on single as well as double resonances in 4D normal-form Hamiltonians, where we visualized classical phase space in a suitable hyperplane. Numerical diagonalization of the quantized normal-form Hamiltonians yielded its eigenstates, whose Husimi representation allowed for the comparison with classical phase-space structures. There, we observed enhanced probability on classical tori located on opposite sides of the resonance channels. In particular, for specific values of the effective Planck's constant, this effect becomes significantly enhanced due to resonance-assisted tunneling. We introduced the weight of an eigenstate localizing on one side of the resonance channel in a disjoint phase-space region as a quantitative measure of tunneling, which gives qualitatively the same behavior as, e.g., phase splittings or tunneling rates studied in a 2D system. That is, we found an overall exponential decay as well as prominent peaks, where tunneling is enhanced over several orders of magnitude, showing a complicated peak structure already for just one double resonance. Furthermore, in this situation suppression of tunneling is possible. This also occurs in 2D systems but only when multiple single resonances are involved, which happens in the deep semiclassical regime in which also small resonance chains become important. This is different in 4D systems, as typically double resonances dominate resonance-assisted tunneling even in the quantum regime of large $\hbar$.

In order to predict the weight and understand the mechanism for the peaks and cases of suppression, the use of the normal-form Hamiltonians allowed us to perform the perturbative calculation in both the single and the double resonance cases. Tunneling across the single resonance turns out to be effectively 2D due to a second constant of motion. In contrast, the situation of the double resonance is more involved. This was visualized by introducing paths on the discrete action grid. There, for the single resonance, just one path needs to be considered, while for the double resonance multiple paths must be included to obtain an accurate description. In particular, this allows for destructive interference of different paths leading to the suppression of tunneling for specific values of $\hbar$. In contrast, the mechanism causing the peaks is the same for both cases and corresponds with the one known from 2D systems. Crucial for enhancement in either case is the energetic degeneracy of action states with respect to the unperturbed Hamiltonian. Note that for different sets of resonance vectors even higher orders of perturbation theory may yield the dominant contribution in comparison with lower orders, i.e., shorter paths. For the concrete systems studied in this paper, this was not the case and it was sufficient to take only the lowest order in terms of the shortest paths into account. Furthermore, we presented a minimal 4×4 matrix model, which captures the observed features of resonance-assisted tunneling in 4D and allowed for a simplified explanation of the observed phenomena.

The perturbative description provides a first step toward a detailed understanding of resonance-assisted tunneling for general higher dimensional systems, e.g., for experimentally feasible three-dimensional optical microcavities or microwave resonators. For a universal description of a generic system, e.g., a 4D quantum map, several presently open problems have to be solved: For example, in phase space the relevant resonances for a given regime of $\hbar$ need to be identified. For these resonances, the parameters for the construction of the normal-form Hamiltonian have to be extracted. Furthermore, for these local approximations of the resonances, a canonical transformation to the phase space of the map needs to be constructed. The subsequent quantization would then allow for a quantitative prediction of the tunneling rates and resonance-assisted tunneling peaks. Beyond that, the development of a semiclassical description only based on the classical properties of the nonlinear resonance would be desirable. Another phenomenon, occurring in at least 4D symplectic maps or 6D Hamiltonians, is the famous Arnold diffusion. It provides a classical transport mechanism connecting different regions in phase space. Its interplay with tunneling is not clear at present.

ACKNOWLEDGMENTS

We are grateful for discussions with Martin Richter and Normann Mertig. Furthermore, we acknowledge support by the Deutsche Forschungsgemeinschaft under Grants No. BA 1973/4-1 and No. KE 537/6-1.

All 3D visualizations were created using MAYAVI [82].

[1] F. Hund, Zur Deutung der Molekelspektren. I, Z. Phys. **40**, 742 (1927).

[2] G. Gamow, Zur Quantentheorie des Atomkernes, Z. Phys. **51**, 204 (1928).

[3] R. W. Gurney and E. U. Condon, Quantum mechanics and radioactive disintegration, Phys. Rev. **33**, 127 (1929).

[4] M. J. Davis and E. J. Heller, Quantum dynamical tunneling in bound states, J. Chem. Phys. **75**, 246 (1981).

[5] S. Keshavamurthy and P. Schlagheck, *Dynamical Tunneling: Theory and Experiment* (Taylor & Francis, Boca Raton, FL, 2011).

[6] W. A. Lin and L. E. Ballentine, Quantum Tunneling and Chaos in a Driven Anharmonic Oscillator, Phys. Rev. Lett. **65**, 2927 (1990).

[7] O. Bohigas, S. Tomsovic, and D. Ullmo, Manifestations of classical phase space structures in quantum mechanics, Phys. Rep. **223**, 43 (1993).

[8] S. Tomsovic and D. Ullmo, Chaos-assisted tunneling, Phys. Rev. E **50**, 145 (1994).

[9] S. Löck, A. Bäcker, R. Ketzmerick, and P. Schlagheck, Regular-to-Chaotic Tunneling Rates: From the Quantum to the Semiclassical Regime, Phys. Rev. Lett. **104**, 114101 (2010).

[10] P. Schlagheck, A. Mouchet, and D. Ullmo, Resonance-assisted tunneling in mixed regular-chaotic systems, in *Dynamical Tunneling: Theory and Experiment* (Taylor & Francis, Boca Raton, FL, 2011), Chap. 8, p. 177.

[11] E. J. Heller, The many faces of tunneling, J. Phys. Chem. A **103**, 10433 (1999).

[12] S. Keshavamurthy, Dynamical tunneling in molecules: quantum routes to energy flow, Int. Rev. Phys. Chem. **26**, 521 (2007).

[13] W. K. Hensinger, H. Häffner, A. Browaeys, N. R. Heckenberg, K. Helmerson, C. McKenzie, G. J. Milburn, W. D. Phillips, S. L. Rolston, H. Rubinsztein-Dunlop, and B. Upcroft, Dynamical tunnelling of ultracold atoms, Nature (London) **412**, 52 (2001).

[14] D. A. Steck, W. H. Oskay, and M. G. Raizen, Observation of chaos-assisted tunneling between islands of stability, Science **293**, 274 (2001).

[15] S. Shinohara, T. Harayama, T. Fukushima, M. Hentschel, T. Sasaki, and E. E. Narimanov, Chaos-Assisted Directional Light Emission from Microcavity Lasers, Phys. Rev. Lett. **104**, 163902 (2010).

[16] S. Shinohara, T. Harayama, T. Fukushima, M. Hentschel, S. Sunada, and E. E. Narimanov, Chaos-assisted emission from asymmetric resonant cavity microlasers, Phys. Rev. A **83**, 053837 (2011).

[17] J. Yang, S.-B. Lee, S. Moon, S.-Y. Lee, S. W. Kim, T. T. A. Dao, J.-H. Lee, and K. An, Pump-Induced Dynamical Tunneling in a Deformed Microcavity Laser, Phys. Rev. Lett. **104**, 243601 (2010).

[18] C.-H. Yi, J. Kullig, C.-M. Kim, and J. Wiersig, Frequency splittings in deformed optical microdisk cavities, Phys. Rev. A **96**, 023848 (2017).

[19] C.-H. Yi, J. Kullig, and J. Wiersig, Pair of Exceptional Points in a Microdisk Cavity under an Extremely Weak Deformation, Phys. Rev. Lett. **120**, 093902 (2018).

[20] J. Kullig and J. Wiersig, Q spoiling in deformed optical microdisks due to resonance-assisted tunneling, Phys. Rev. E **94**, 022202 (2016).

[21] H. Kwak, Y. Shin, S. Moon, S.-B. Lee, J. Yang, and K. An, Nonlinear resonance-assisted tunneling induced by microcavity deformation, Sci. Rep. **5**, 9010 (2015).

[22] C. Dembowski, H.-D. Gräf, A. Heine, R. Hofferbert, H. Rehfeld, and A. Richter, First Experimental Evidence for Chaos-Assisted Tunneling in a Microwave Annular Billiard, Phys. Rev. Lett. **84**, 867 (2000).

[23] A. Bäcker, R. Ketzmerick, S. Löck, M. Robnik, G. Vidmar, R. Höhmann, U. Kuhl, and H.-J. Stöckmann, Dynamical Tunneling in Mushroom Billiards, Phys. Rev. Lett. **100**, 174103 (2008).

[24] B. Dietz, T. Guhr, B. Gutkin, M. Miski-Oglu, and A. Richter, Spectral properties and dynamical tunneling in constant-width billiards, Phys. Rev. E **90**, 022903 (2014).

[25] A. Bäcker, R. Ketzmerick, S. Löck, and N. Mertig, Fractional-Power-Law Level Statistics Due to Dynamical Tunneling, Phys. Rev. Lett. **106**, 024101 (2011).

[26] A. M. Ozorio de Almeida, Tunneling and the semiclassical spectrum for an isolated classical resonance, J. Phys. Chem. **88**, 6139 (1984).

[27] O. Brodier, P. Schlagheck, and D. Ullmo, Resonance-Assisted Tunneling in Near-Integrable Systems, Phys. Rev. Lett. **87**, 064101 (2001).

[28] O. Brodier, P. Schlagheck, and D. Ullmo, Resonance-assisted tunneling, Ann. Phys. (NY) **300**, 88 (2002).

[29] S. Gehler, S. Löck, S. Shinohara, A. Bäcker, R. Ketzmerick, U. Kuhl, and H.-J. Stöckmann, Experimental Observation of Resonance-Assisted Tunneling, Phys. Rev. Lett. **115**, 104101 (2015).

[30] A. Shudo and K. S. Ikeda, Complex Classical Trajectories and Chaotic Tunneling, Phys. Rev. Lett. **74**, 682 (1995).

[31] A. Shudo and K. S. Ikeda, Chaotic tunneling: A remarkable manifestation of complex classical dynamics in non-integrable quantum phenomena, Physica D **115**, 234 (1998).

[32] V. A. Podolskiy and E. E. Narimanov, Semiclassical Description of Chaos-Assisted Tunneling, Phys. Rev. Lett. **91**, 263601 (2003).

[33] S. Keshavamurthy, Dynamical tunneling in molecules: Role of the classical resonances and chaos, J. Chem. Phys. **119**, 161 (2003).

[34] V. A. Podolskiy and E. E. Narimanov, Chaos-assisted tunneling in dielectric microcavities, Opt. Lett. **30**, 474 (2005).

[35] C. Eltschka and P. Schlagheck, Resonance- and Chaos-Assisted Tunneling in Mixed Regular-Chaotic Systems, Phys. Rev. Lett. **94**, 014101 (2005).

[36] S. Keshavamurthy, On dynamical tunneling and classical resonances, J. Chem. Phys. **122**, 114109 (2005).

[37] M. Sheinman, S. Fishman, I. Guarneri, and L. Rebuzzini, Decay of quantum accelerator modes, Phys. Rev. A **73**, 052110 (2006).

[38] A. Bäcker, R. Ketzmerick, S. Löck, and L. Schilling, Regular-to-Chaotic Tunneling Rates using a Fictitious Integrable System, Phys. Rev. Lett. **100**, 104101 (2008).

[39] A. Shudo and K. S. Ikeda, Stokes geometry for the quantum Hénon map, Nonlinearity **21**, 1831 (2008).

[40] A. Shudo, Y. Ishii, and K. S. Ikeda, Chaos attracts tunneling trajectories: A universal mechanism of chaotic tunneling, Europhys. Lett. **81**, 50003 (2008).

[41] A. Shudo, Y. Ishii, and K. S. Ikeda, Julia sets and chaotic tunneling: I, J. Phys. A **42**, 265101 (2009).

[42] A. Shudo, Y. Ishii, and K. S. Ikeda, Julia sets and chaotic tunneling: II, J. Phys. A **42**, 265102 (2009).

[43] A. Bäcker, R. Ketzmerick, S. Löck, J. Wiersig, and M. Hentschel, Quality factors and dynamical tunneling in annular microcavities, Phys. Rev. A **79**, 063804 (2009).

[44] A. Bäcker, R. Ketzmerick, and S. Löck, Direct regular-to-chaotic tunneling rates using the fictitious-integrable-system approach, Phys. Rev. E **82**, 056208 (2010).

[45] N. Mertig, S. Löck, A. Bäcker, R. Ketzmerick, and A. Shudo, Complex paths for regular-to-chaotic tunnelling rates, Europhys. Lett. **102**, 10005 (2013).

[46] Y. Hanada, A. Shudo, and K. S. Ikeda, Origin of the enhancement of tunneling probability in the nearly integrable system, Phys. Rev. E **91**, 042913 (2015).

[47] A. Shudo and K. S. Ikeda, Toward pruning theory of the Stokes geometry for the quantum Hénon map, Nonlinearity **29**, 375 (2016).

[48] N. Mertig, J. Kullig, C. Löbner, A. Bäcker, and R. Ketzmerick, Perturbation-free prediction of resonance-assisted tunneling in mixed regular-chaotic systems, Phys. Rev. E **94**, 062220 (2016).

[49] F. Fritzsch, A. Bäcker, R. Ketzmerick, and N. Mertig, Complex-path prediction of resonance-assisted tunneling in mixed systems, Phys. Rev. E **95**, 020202(R) (2017).

[50] P. Lebœuf and A. Mouchet, Normal forms and complex periodic orbits in semiclassical expansions of Hamiltonian systems, Ann. Phys. (NY) **275**, 54 (1999).

[51] S. Creagh, Tunnelling in multidimensional systems, J. Phys. A **27**, 4969 (1994).

[52] S. Keshavamurthy, Resonance-assisted tunneling in three degrees of freedom without discrete symmetry, Phys. Rev. E **72**, 045203(R) (2005).

[53] M. Richter, Classical and quantum investigations of four-dimensional maps with a mixed phase space, Ph.D. thesis, Technische Universität Dresden, Fachrichtung Physik, Dresden, Germany, 2012, http://nbn-resolving.de/urn:nbn:de:bsz:14-qucosa-91420.

[54] S. M. Pittman, E. Tannenbaum, and E. J. Heller, Dynamical tunneling versus fast diffusion for a non-convex Hamiltonian, J. Chem. Phys. **145**, 054303 (2016).

[55] S. Karmakar and S. Keshavamurthy, Relevance of the resonance junctions on the Arnold web to dynamical tunneling and eigenstate delocalization, J. Phys. Chem. A **122**, 8636 (2018).

[56] G. H. Walker and J. Ford, Amplitude instability and ergodic behavior for conservative nonlinear oscillator systems, Phys. Rev. **188**, 416 (1969).

[57] E. Todesco, Analysis of resonant structures of four-dimensional symplectic mappings, using normal forms, Phys. Rev. E **50**, R4298 (1994).

[58] G. Haller, Universal homoclinic bifurcations and chaos near double resonances, J. Stat. Phys. **86**, 1011 (1997).

[59] G. Haller, *Chaos Near Resonance*, Applied Mathematical Sciences, Vol. 138 (Springer, New York, 1999).

[60] V. Gelfreich, C. Simó, and A. Vieiro, Dynamics of symplectic maps near a double resonance, Physica D **243**, 92 (2013).

[61] R. T. Swimm and J. B. Delos, Semiclassical calculations of vibrational energy levels for nonseparable systems using the Birkhoff-Gustavson normal form, J. Chem. Phys. **71**, 1706 (1979).

[62] T. Uzer and W. H. Miller, Theories of intramolecular vibrational energy transfer, Phys. Rep. **199**, 73 (1991).

[63] M. Gruebele, Quantum dynamics and control of vibrational dephasing, J. Phys.: Condens. Matter **16**, R1057 (2004).

[64] A. Semparithi and S. Keshavamurthy, Intramolecular vibrational energy redistribution in DCO ($\tilde{X}^2A'$): Classical-quantum correspondence, dynamical assignments of highly excited states, and phase space transport, Phys. Chem. Chem. Phys. **5**, 5051 (2003).

[65] A. Semparithi and S. Keshavamurthy, Parametric perspective on highly excited states: Case studies of CHBrClF and C_2H_2, Chem. Phys. Lett. **395**, 327 (2004).

[66] S. Keshavamurthy and G. S. Ezra, Eigenstate assignments and the quantum-classical correspondence for highly excited vibrational states of the Baggot H_2O Hamiltonian, J. Chem. Phys. **107**, 156 (1997).

[67] S. C. Farantos, R. Schinke, H. Guo, and M. Joyeux, Energy localization in molecules, bifurcation phenomena, and their spectroscopic signatures: The global view, Chem. Rev. **109**, 4248 (2009).

[68] S. Keshavamurthy, Scaling perspective on intramolecular vibrational energy flow, in *Advances in Chemical Physics*, edited by S. A. Rice and A. R. Dinner (John Wiley & Sons, New York, 2013).

[69] D. M. Leitner, Quantum ergodicity and energy flow in molecules, Adv. Phys. **64**, 445 (2015).

[70] M. E. Kellman, Approximate constants of motion for vibrational spectra of many-oscillator systems with multiple anharmonic resonances, J. Chem. Phys. **93**, 6630 (1990).

[71] A. J. Lichtenberg and M. A. Lieberman, *Regular and Chaotic Dynamics*, 2nd ed. (Springer-Verlag, New York, 1992).

[72] F. Onken, S. Lange, R. Ketzmerick, and A. Bäcker, Bifurcations of families of 1D-tori in 4D symplectic maps, Chaos **26**, 063124 (2016).

[73] M. Richter, S. Lange, A. Bäcker, and R. Ketzmerick, Visualization and comparison of classical structures and quantum states of four-dimensional maps, Phys. Rev. E **89**, 022902 (2014).

[74] H. J. Groenewold, On the principles of elementary quantum mechanics, Physica **12**, 405 (1946).

[75] F. Bloch, Über die Quantenmechanik der Elektronen in Kristallgittern, Z. Phys. **52**, 555 (1929).

[76] K. Husimi, Some formal properties of the density matrix, Proc. Phys. Math. Soc. Jpn. **22**, 264 (1940).

[77] S. Nonnenmacher and A. Voros, Chaotic eigenfunctions in phase space, J. Stat. Phys. **92**, 431 (1998).

[78] P.-O. Löwdin, A note on the quantum-mechanical perturbation theory, J. Chem. Phys. **19**, 1396 (1951).

[79] J. E. Howard and R. S. MacKay, Linear stability of symplectic maps, J. Math. Phys. **28**, 1036 (1987).

[80] E. Todesco, Local analysis of formal stability and existence of fixed points in 4d symplectic mappings, Physica D **95**, 1 (1996).

[81] S. Löck, Dynamical tunneling in systems with a mixed phase space, Ph.D. thesis, Technische Universität Dresden, Fachrichtung Physik, Dresden, Germany, 2010, http://nbn-resolving.de/urn:nbn:de:bsz:14-qucosa-33335.

[82] P. Ramachandran and G. Varoquaux, MAYAVI: 3D visualization of scientific data, Comput. Sci. Eng. **13**, 40 (2011).